Precise study of the final-state continua in ^{8}Li and ^{8}B decays

M. Bhattacharya,* E. G. Adelberger, and H. E. Swanson
Center for Experimental Nuclear Physics and Astrophysics, University of Washington, Seattle, Washington 98195-4290, USA
(Received 16 December 2005; published 19 May 2006)

We studied β-delayed singles-α spectra from ^{8}Li and ^{8}B decays with special emphasis on a careful calibration of the energy scale. ^{8}Li and ^{8}B activities were produced by ^{7}Li(d, p) and ^{6}Li(^{3}He,n) reactions, respectively, and deposited in thin C foils. Delayed α's were counted in thin, cooled Si detectors with small solid angles to reduce summing with β's. The energy scale and detector response were calibrated with spectroscopic grade radioactive sources. We extracted the ^{8}Li and ^{8}B final-state continuum shapes from our spectra by using R-matrix analyses that included effects of lepton-recoil broadening and detector response. Our results are in excellent agreement with a recent measurement using ^{8}B's implanted in a Si counter and in good agreement with our reanalysis of the older Wilkinson-Alburger ^{8}Li and ^{8}B data, but disagree with a recent ^{8}B experiment using a coincidence technique.

DOI: 10.1103/PhysRevC.73.055802 PACS number(s): 23.40.−s, 23.60.+e, 27.20.+n

I. INTRODUCTION

The shapes of the broad ^{8}Be final-state continua populated in ^{8}Li and ^{8}B β decays are interesting from a nuclear physics perspective. But, more important, the ^{8}B β final-state distribution determines the intrinsic spectrum of ^{8}B neutrinos that dominate the counting rates of the Kamiokande [1], Super-Kamiokande [2] and SNO [3,4] solar neutrino detectors and form a major component of the Homestake detector [5] events. Precise knowledge of this undistorted spectrum is needed to extract as much information as possible about neutrino oscillation parameters from the observed spectrum of solar neutrinos detected on Earth.

The $J^\pi = 2^+$ ^{8}Li and ^{8}B ground states decay to a 2^+ continuum in ^{8}Be that very rapidly breaks up into 2 α particles. The only other energetically allowed β decays are second-forbidden transitions to 0^+ or 4^+ states that can be neglected. The 2^+ continuum is dominated by a ^{8}Be state at 3 MeV with a width of 1.5 MeV. The interference of this very broad state with other 2^+ states at higher energies affects the shapes of the final-state continuum and therefore the shape of the β and neutrino spectra. As a result, high-quality measurements of the final-state continuum are needed for accurate computation of the neutrino spectrum.

The ^{8}Li and ^{8}B final-state continua can be inferred from either β spectra or β-delayed α spectra. Bahcall *et al.* [6] showed that the existing ^{8}B singles delayed-α spectra [7–9] were inconsistent with one another: the spectrum peaks in the different experiments varied by $\pm$80 keV. Because of this inconsistency, Bahcall *et al.* [6] used the single available β spectrum-shape measurement [10] to infer their standard ^{8}B neutrino spectrum.

We have shown [11] that lepton recoil, which had been neglected in all previous analyses of the $A = 8$ delayed-α shapes, perceptibly distorts the singles-α spectrum shapes and therefore the extracted β final-state distributions. Accounting for lepton recoil significantly reduced the discrepancies previously noted [12–14] between the delayed-α shapes in ^{8}Li and ^{8}B decays and for the $L = 2$ phase shifts in $\alpha + \alpha$ scattering.

Recently, Ortiz *et al.* [15,16] used a new technique to study the ^{8}B delayed-α spectrum with high precision. They placed a pair of oppositely facing detectors in a strong magnetic field to prevent the associated β's from reaching the detectors and measured the summed energy of the two coincident delayed α's. This eliminated the first-order effect of lepton-recoil broadening. However, the magnetic field gave the coincidence α-detection efficiency a dependence on the ^{8}B excitation energy, which had to be accounted for with a Monte Carlo simulation. Still more recently, Winter *et al.* [17,18] made a precise study of the ^{8}B delayed-α spectrum by a different method, but one which also measured the summed energy of the two α's. Winter *et al.* implanted 27.3 MeV ^{8}B's into a thin Si counter and detected the decay positrons in a plastic scintillator. The plastic scintillator coincidence selected events where positrons traveled within 30° of the detector normal to minimize the energy deposited by the positrons. However, these two results of nominally similar precision disagreed. Although the disagreement was smaller than that noted previously by Bahcall *et al.*, it was nevertheless significant, considering the increasing precision of the solar neutrino data.

This paper reports a precise measurement of the delayed-α continua in ^{8}B and ^{8}Li decays performed by using a conventional singles-α technique (rather than the summed-α techniques employed in Refs. [15] and [17,18]. Our data were taken and analyzed after the publication of Ref. [15] but before that of Ref. [17].

II. EXPERIMENTAL PROCEDURE

A. Apparatus

Figure 1 shows a schematic diagram of our apparatus; details can be found in Ref. [19]. The ^{8}Li and ^{8}B activities were produced via ^{7}Li(d, p) and ^{6}Li(^{3}He,n) reactions at

*Present address: E-39 Von Braun Research Hall, University of Alabama in Huntsville, 301 Sparkman Drive, Huntsville, Al 35899; Electronic address: bhattmx@nsstc.uah.edu

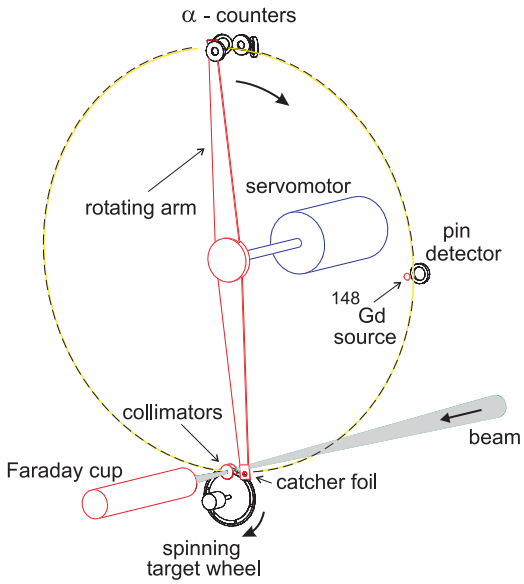

FIG. 1. (Color online) Schematic diagram of our apparatus.

bombarding energies of 1.0 and 5.5 MeV, respectively. The University of Washington tandem accelerator fitted with a terminal ion source delivered ~16 μA 1.0 MeV d and ~12 μA 5.5 MeV $^3He^+$ beams through a 3.2 mm diameter collimator. These beams struck spinning targets to reduce the target heating; the recoiling ^{8}Li and ^{8}B nuclei were implanted into 11.1-mm-diameter carbon catcher foils located directly behind the target. The catcher foils for the ^{8}Li and ^{8}B runs had nominal thicknesses of 10 and 20 μg/cm^2, respectively. The target for the ^{8}Li run consisted of ^{nat}LiF evaporated onto the downstream side of a nickel backing; for the ^{8}B run we evaporated ^{6}LiF onto the downstream side of a copper foil for better heat conductivity.

The catcher foils were attached to the ends of a 37-cm-radius arm that rotated 180° to cycle the foils from the bombardment station to the counting station and back again. Targets were bombarded for 2.00 s. The beam was then switched off by a fast magnet during the rotation and counting periods, which had durations of 0.15 and 5.00 s, respectively. The catcher foils were viewed on opposite sides by a pair of 75-μm-thick, 150-mm^2 silicon surface barrier (SSB) detectors (E counters) that were tightly collimated ($\Delta\Omega/4\pi = 2.2 \times 10^{-3}$) to minimize the energy summing of the α's with the preceding β's.

Two additional 75-μm-thick SSB detectors, at 45° on either side of one of the E counters, were operated in coincidence with the two E counters. These provided us with E-counter β spectra that were used for low-energy β-background subtraction as described below. All detectors were operated at 0°C to reduce leakage currents, and our amplifiers, pulser, and ADC's were mounted in a temperature-controlled rack for improved stability of the energy calibration.

B. Delayed-α data collection

The two E counters and the two 45° counters fed timing single-channel analyzers with thresholds set just above the noise. Data acquisition was triggered by an output of any of the single-channel analyses, in which case all detectors were read out. Counting rates were low enough that random coincidences were negligible. For each event we recorded the time interval between the start of the counting cycle, i.e., the arrival of a catcher foil at the counting station, and a signal in any one of our detectors. This was done by reading a 1 kHz clock that was zeroed every time fresh radioactivity was positioned at the counting station.

III. CALIBRATIONS

A. Energy scale and detector response

We placed special emphasis on the energy calibration. The linearity and zero point of our energy scale were determined with a precision pulser. The absolute scale factor was calibrated with high-resolution, spectroscopic-grade ^{148}Gd, ^{239}Pu, and ^{241}Am α sources [20] that were periodically placed in front of the detectors without breaking vacuum. The energies of these α decays were taken from Ref. [21].

We fitted the α source peaks (see Fig. 2) with an analytic function consisting of a Gaussian folded through two low-energy exponential tails:

$$R(E, E') = \sum_{i=1}^{2} \frac{A_i}{2\lambda_i} \exp\left[\frac{(E-E')}{\lambda_i} + \frac{\sigma^2}{2\lambda_i^2}\right] \times \mathrm{erfc}\left(\frac{E-E'+\sigma^2/\lambda_i}{\sqrt{2}\sigma}\right), \quad (1)$$

where E and E' are the nominal and observed energies of the peak, $\sigma = \mathrm{FWHM}/(8\log 2)$, $\lambda_{1(2)}$ are exponential decay lengths ($\lambda_1 < \lambda_2$), and erfc is the complement of the incomplete error function. The normalization coefficients are $A_1 = 1/(1+r)$ and $A_2 = r/(1+r)$ with r the relative area of tail 2 compared with tail 1. We used two measures of the peak position: E_c and E_c^1. The centroid of the entire peak is $E_c = E - A_1\lambda_1 - A_2\lambda_2$, while the centroid of the peak including the effect of tail 1 alone is $E_c^1 = E - A_1\lambda_1$. We found (see below) that tail 2 depended much more strongly on

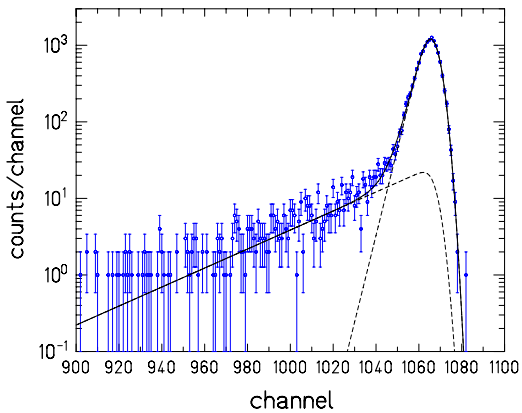

FIG. 2. (Color online) Lineshape fit of the ^{148}Gd peak in detector 1. The dashed curves show the contributions of the short and long tails, while the solid curve shows their sum.

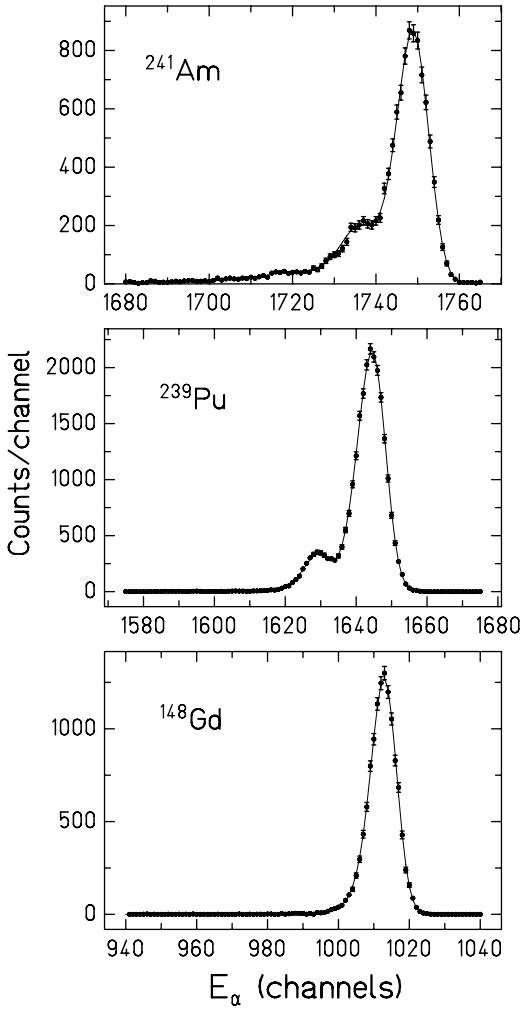

FIG. 3. Alpha particle spectra and lineshape fits for the ^{148}Gd and ^{239}Pu and ^{241}Am sources. The ^{241}Am line and the ^{239}Pu line are triplets.

the angle of the α's with respect to the detector than on their angle with respect to the source.

The α source thicknesses were determined at the end of the experiment by studying the shifts in the line spectra as the sources were rotated about their axes. Figure 3 shows sample source spectra. We determined the mean thicknesses of our sources from a linear fit of E_c^1 as a function of the secant of the source angle θ_s. Figure 4 displays our data for the ^{148}Gd source. We used E_c^1 (rather than E_c) as a measure of peak position in this determination because tail 2 was relatively poorly determined by our data and (owing to its length) had a disproportionate effect on E_c, giving unnecessary scatter. The mean energy losses of the most intense lines in the ^{148}Gd (3182.7 keV), ^{239}Pu (5156.6 keV), and ^{241}Am (5485.6 keV) sources were 4.2, 2.2, and 4.6 keV, respectively.

Detector dead-layer thicknesses were measured by using a special jig that rotated an α source by an angle θ_d in an arc centered on the detectors. Results for one detector are shown in Fig. 5. In this case we analyzed E_c versus $\sec\theta_d$ data because the detector dead layer was responsible for most of tail 2. The measured dead-layer thicknesses of the two

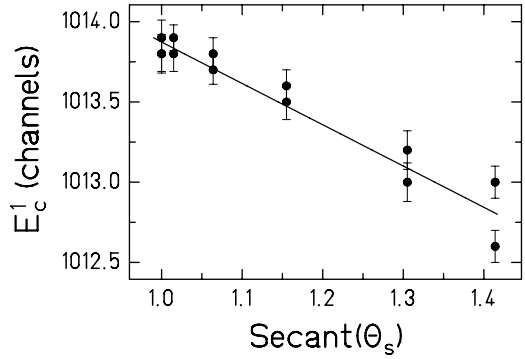

FIG. 4. Source thickness measurement showing the ^{148}Gd peak position as a function of the source rotation angle. These data were taken with detector 1.

E counters were quite different: 58.7 ± 4.9 and 41.2 ± 1.8 μg/cm^2, respectively, where we assumed that the dead layers were gold. The nominal gold dead layer specified by the manufacturer is 40 μg/cm^2.

We used the α-source data, along with the zero-energy point determined with a precision pulser, to establish the energy calibration. The actual α energies deposited in the detectors, accounting for energy losses in the sources and detector dead layers, were fitted as linear functions of the E_c positions of the peaks (which had very small uncertainties). The fit residuals were $\pm$3.0 and $\pm$2.7 keV for detectors E1 and E2, respectively (see Fig. 6). Figure 7 shows that the gain of our system was quite stable, typically varying by 0.04% over 7 days of data taking. We therefore assign systematic errors of $\pm$3 keV and $\pm$6 keV to our α particle and excitation energies, respectively.

B. Catcher foil thickness

A PIN detector and ^{148}Gd alpha source permanently mounted in the vacuum chamber allowed us to periodically monitor the catcher foil thickness by rotating the arm by 90° to place the foil between the source and the PIN detector. Typical measured foil thicknesses for the ^{8}Li (^{8}B) run were 14.5 (23.5) μg/cm^2, increasing by 4.5% (2.8%) after 18 h of bombardment.

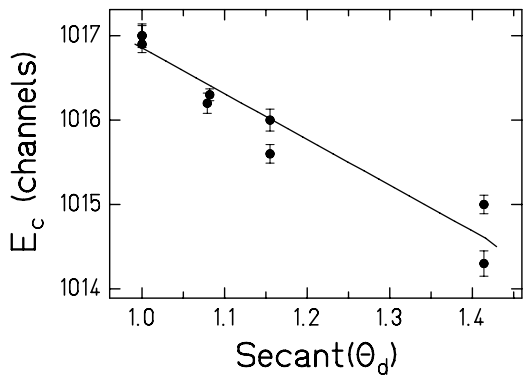

FIG. 5. Measurement of the dead layer of detector 1, showing the ^{148}Gd peak position as a function of the source position.

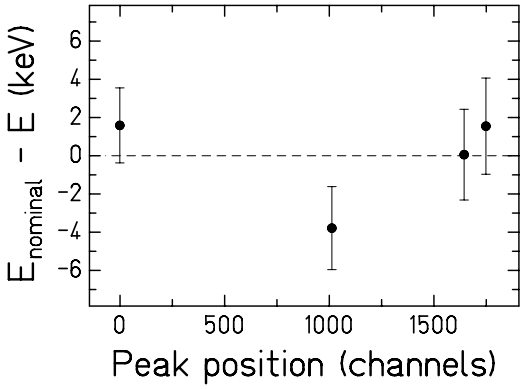

FIG. 6. Energy calibration of detector 1, showing residuals from a linear fit. Uncertainties in the peak positions were negligible compared with the uncertainties of the actual α energy deposited in the detector.

IV. DATA REDUCTION AND ANALYSIS

A. Decay-time spectra

We generated E-counter decay-time spectra by gating on pulse heights just above the valley between the falling β background and the rising α's and sorted the results according to the time signal from the 1 kHz clock that was reset every bombardment cycle. Results are shown in Fig. 8. These time spectra were fitted with a decaying exponential plus a constant to account for any long-lived β activities. The best-fit exponential time constants were in good agreement with tabulated values [22] for ^{8}Li and ^{8}B decays.

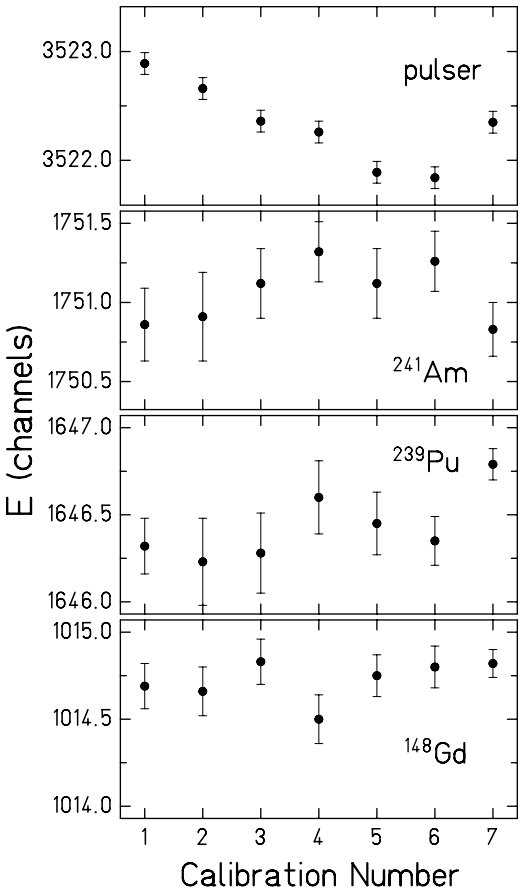

FIG. 7. Stability of the energy calibrations. Top panel, raw position of the pulser peak; lower 3 panels, positions of the pulser-corrected peaks from the α sources. Calibrations 1–6 were taken during 5 days of ^{8}B delayed-α data. Calibration 7 occurred between 1 and 2 days after the β-decay data taking was completed.

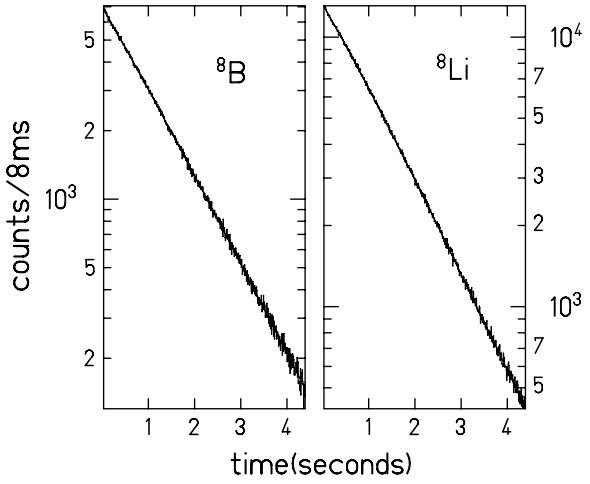

FIG. 8. Decay-time spectra for events with energies >860 keV, from ^{8}B (left panel) and ^{8}Li (right panel) decays. The data were fitted with a single decaying exponential. The best-fit half-lives extracted from the ^{8}Li (^{8}B) data are 832.5 ± 8.4 ms (747.5 ± 27.5 ms), which agree with the tabulated values [22] of 840 ± 2 ms (770 ± 3 ms).

B. Delayed-α energy spectra

We sorted the delayed-α data into early (first 2 s of the counting period) and late (last 2 s of the counting period) spectra and subtracted the late-time spectra from the early-time spectra to minimize the low-energy background from long-lived β activity. We then used the β events in our E counters in coincidence with α's in our 45° counters to subtract the low-energy β backgrounds from the decay of ^{8}Li and ^{8}B themselves. The β-subtracted spectra were first gain shifted to place the pulser peak in the same channel for all runs (the pulser peaks were quite stable, drifting by no more than 0.02% over the course of week long runs). We then converted channel numbers into delayed-α energies deposited into the counter by using the calibrations based on a linear fit of the zero-energy point and the three α-source peaks, taking into account the source thicknesses and detector dead layers. We then corrected for the energy loss of the delayed α's in the catcher foil and detector dead layer. Finally, individual runs for each detector were added and then rebinned into excitation-energy spectra with 100 keV-wide bins, taking into account that the ^{8}Be ground state is unbound by 92 keV. The results are shown in Fig. 9.

C. Analysis of the delayed-α spectra

We analyzed our excitation-energy distributions by using essentially the same procedure (and notation) we used in Ref. [11]. We employed Warburton's version [14] of the

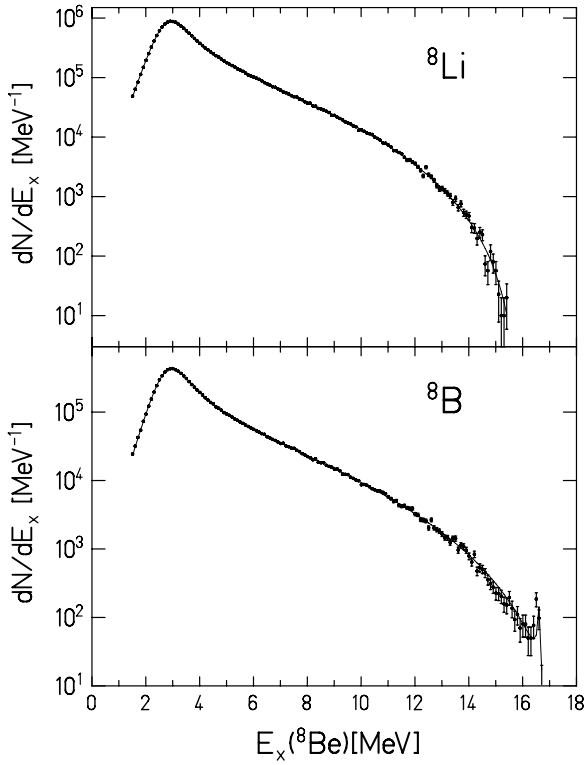

FIG. 9. Data and R-matrix fits from this work. Upper panel, ^{8}Li delayed-α spectrum containing a total of 1.86 million counts. Lower panel, ^{8}B delayed-α spectrum with a total of 0.95 million counts.

one-channel, many-level R-matrix formalism as cited in Ref. [11] and a channel radius of 4.50 fm. The statistical rate function $f(E_\beta)$ was evaluated by using the prescription of Wilkinson and Macefield [23]. Following Warburton and our Ref. [11], the final-state continuum was decomposed into three physical levels, the broad 3 MeV state and the narrow doublet at 16.626 and 16.922 MeV, plus a background level at $E_x = 37$ MeV. The R-matrix shape was then folded with the first-order lepton-recoil broadening function described in Ref. [11] and with the detector response function given in Eq. (1), whose parameters were chosen to fit data from our high-resolution ^{148}Gd source (see Fig. 2). Ideally, a small second-order lepton-recoil correction should be applied to account for the mean energy shift

$$\langle \Delta E \rangle = \frac{1}{2N}\frac{mc^2}{(Mc^2)^2}\int_{mc^2}^{E_0} dE F(E,A,Z) pE(E_0-E)^2 \times \left[p^2 + (E_0-E)^2 + \frac{4ap^2}{3E}(E_0-E)\right], \quad (2)$$

where E_0 is the endpoint energy, E and p are the β total energy and momentum, m and M are the α and final-state ^{8}Be masses, $a = -1/3$ is the e-ν correlation for an allowed Gamow-Teller transition, F is the Fermi function, and

$$N = \int_{mc^2}^{E_0} dE F(E,A,Z) pE(E_0-E)^2. \quad (3)$$

However, the mean energy shifts are almost negligible—in ^{8}B (^{8}Li) decay $\langle \Delta E \rangle$ is 3.3 (2.9), 2.1 (1.8), and 1.1 (0.9) keV for ^{8}Be excitation energies of 3, 6, and 9 MeV respectively—and were ignored in our analysis. The folded R-matrix function was then fitted to our data, the adjustable parameters being the energy and width of the 3-MeV level, the width of the background level, the GT matrix elements feeding the 3 MeV level (M_1), the $T = 0$ component of the doublet (M_{2+3}), and the background state (M_4). The energies and widths of the 16 MeV doublet levels were fixed at their accepted values [22]. The fits to our ^{8}Li and ^{8}B delayed-α spectra are shown in Fig. 9, and their R-matrix parameters are listed in Tables II and III below.

D. Final-state distributions and their uncertainties

Our ^{8}Li and ^{8}B β-decay final-state distributions as functions of E_x in ^{8}Be are shown in Table I and in Figs. 10, 11, and 12 below. These were computed from the best-fit R-matrix parameters given in Table III below. The uncertainties have two sources: errors arising from the R-matrix parametrization of our spectra, and uncertainties in the energy calibration of the spectra.

For a fixed R-matrix matching radius, the uncertainty from the R-matrix parametrization (computed by using the full covariance matrix of the fit parameters) was negligible compared with the systematic error described below. (The different R-matrix parameters were highly correlated, so one cannot infer the uncertainties in the final-state distribution from the diagonal covariance elements alone.) However, a significant error from the R-matrix parametrization arises because of the ambiguity in the proper choice of matching radius. We chose a reasonable range of matching radii to be between $R^- = 4.2$ fm and $R^+ = 4.8$ fm by requiring the total χ^2 not to vary more than 1 unit from its minimum value at $R^0 = 4.5$ fm. We computed the corresponding final-state distributions $(dN/dE_x)_{R^-}$ and $(dN/dE_x)_{R^+}$ and compared

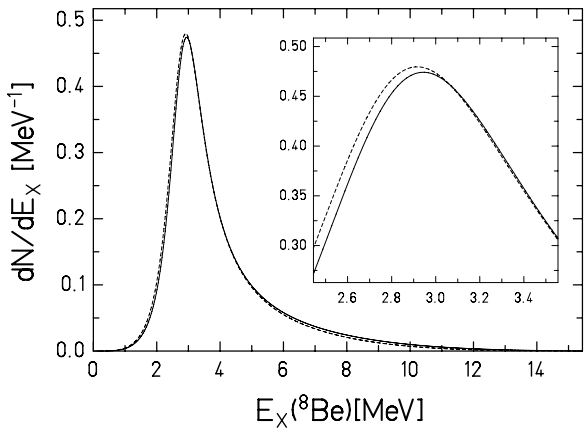

FIG. 10. Comparison of the ^{8}Li final-state continuum shapes that we extract from R-matrix analyses of our α spectrum (solid curve) and a previous spectrum of Wilkinson and Alburger [7] (dashed curve). Both shapes have been normalized to the same total area. The continuum shapes obtained by fitting the Wilkinson-Alburger data are described in Ref. [11]. The inset shows an expanded view of the peak region where the difference between the two data sets is most easily visible.

TABLE I. ^{8}B final-state distribution normalized to unit area, dN/dE_x, from this work. Excitation energies are in MeV and final-state distributions are in GeV^{-1}. Statistical errors are negligible. σ_E and σ_R are systematic errors due to energy calibrations and the R-matrix parametrization, respectively. Our ^{8}B and ^{8}Li final-state distributions at 20 keV intervals are archived at Ref. [24].

E_x	$dN/dE_x \pm \sigma_E \pm \sigma_R$	E_x	$dN/dE_x \pm \sigma_E \pm \sigma_R$	E_x	$dN/dE_x \pm \sigma_E \pm \sigma_R$	E_x	$dN/dE_x \pm \sigma_E \pm \sigma_R$
0.2	$0.005 \pm 0.000 \pm 0.000$	4.4	$146.574 \pm 0.452 \pm 0.452$	8.6	$18.673 \pm 0.093 \pm 0.059$	12.8	$2.077 \pm 0.025 \pm 0.019$
0.4	$0.088 \pm 0.001 \pm 0.002$	4.6	$127.239 \pm 0.389 \pm 0.436$	8.8	$17.096 \pm 0.091 \pm 0.056$	13.0	$1.815 \pm 0.024 \pm 0.017$
0.6	$0.472 \pm 0.004 \pm 0.013$	4.8	$111.598 \pm 0.345 \pm 0.396$	9.0	$15.638 \pm 0.088 \pm 0.058$	13.2	$1.579 \pm 0.022 \pm 0.019$
0.8	$1.534 \pm 0.010 \pm 0.036$	5.0	$98.735 \pm 0.315 \pm 0.345$	9.2	$14.290 \pm 0.085 \pm 0.059$	13.4	$1.366 \pm 0.021 \pm 0.020$
1.0	$3.836 \pm 0.019 \pm 0.076$	5.2	$87.993 \pm 0.294 \pm 0.286$	9.4	$13.043 \pm 0.082 \pm 0.059$	13.6	$1.175 \pm 0.019 \pm 0.020$
1.2	$8.236 \pm 0.031 \pm 0.132$	5.4	$78.898 \pm 0.278 \pm 0.226$	9.6	$11.891 \pm 0.078 \pm 0.057$	13.8	$1.004 \pm 0.019 \pm 0.019$
1.4	$16.094 \pm 0.044 \pm 0.201$	5.6	$71.102 \pm 0.261 \pm 0.168$	9.8	$10.826 \pm 0.074 \pm 0.055$	14.0	$0.852 \pm 0.017 \pm 0.018$
1.6	$29.640 \pm 0.052 \pm 0.265$	5.8	$64.342 \pm 0.248 \pm 0.112$	10.0	$9.843 \pm 0.070 \pm 0.050$	14.2	$0.717 \pm 0.016 \pm 0.017$
1.8	$52.586 \pm 0.049 \pm 0.288$	6.0	$58.426 \pm 0.233 \pm 0.073$	10.2	$8.935 \pm 0.065 \pm 0.046$	14.4	$0.599 \pm 0.014 \pm 0.017$
2.0	$90.945 \pm 0.084 \pm 0.202$	6.2	$53.202 \pm 0.218 \pm 0.067$	10.4	$8.097 \pm 0.061 \pm 0.042$	14.6	$0.495 \pm 0.013 \pm 0.016$
2.2	$153.294 \pm 0.232 \pm 0.085$	6.4	$48.556 \pm 0.201 \pm 0.060$	10.6	$7.326 \pm 0.056 \pm 0.039$	14.8	$0.404 \pm 0.011 \pm 0.013$
2.4	$246.927 \pm 0.387 \pm 0.591$	6.6	$44.394 \pm 0.185 \pm 0.050$	10.8	$6.615 \pm 0.052 \pm 0.040$	15.0	$0.326 \pm 0.010 \pm 0.012$
2.6	$362.249 \pm 0.245 \pm 0.950$	6.8	$40.645 \pm 0.170 \pm 0.072$	11.0	$5.963 \pm 0.047 \pm 0.042$	15.2	$0.259 \pm 0.009 \pm 0.010$
2.8	$453.659 \pm 0.909 \pm 0.526$	7.0	$37.251 \pm 0.156 \pm 0.089$	11.2	$5.363 \pm 0.043 \pm 0.042$	15.4	$0.202 \pm 0.007 \pm 0.008$
3.0	$471.755 \pm 1.400 \pm 0.318$	7.2	$34.165 \pm 0.143 \pm 0.100$	11.4	$4.812 \pm 0.040 \pm 0.040$	15.6	$0.155 \pm 0.006 \pm 0.007$
3.2	$425.495 \pm 1.444 \pm 0.635$	7.4	$31.350 \pm 0.129 \pm 0.105$	11.6	$4.307 \pm 0.038 \pm 0.038$	15.8	$0.117 \pm 0.005 \pm 0.006$
3.4	$357.259 \pm 1.261 \pm 0.423$	7.6	$28.772 \pm 0.120 \pm 0.105$	11.8	$3.845 \pm 0.034 \pm 0.036$	16.0	$0.086 \pm 0.004 \pm 0.005$
3.6	$293.626 \pm 1.028 \pm 0.197$	7.8	$26.407 \pm 0.112 \pm 0.101$	12.0	$3.423 \pm 0.032 \pm 0.033$	16.2	$0.063 \pm 0.003 \pm 0.003$
3.8	$242.047 \pm 0.836 \pm 0.185$	8.0	$24.231 \pm 0.106 \pm 0.095$	12.2	$3.037 \pm 0.030 \pm 0.029$	16.4	$0.050 \pm 0.003 \pm 0.002$
4.0	$201.943 \pm 0.672 \pm 0.349$	8.2	$22.228 \pm 0.100 \pm 0.084$	12.4	$2.686 \pm 0.028 \pm 0.026$	16.6	$0.126 \pm 0.010 \pm 0.020$
4.2	$170.884 \pm 0.546 \pm 0.428$	8.4	$20.379 \pm 0.097 \pm 0.072$	12.6	$2.367 \pm 0.026 \pm 0.023$	16.8	$0.000 \pm 0.000 \pm 0.001$

them with $(dN/dE_x)_{R^0}$ to obtain the R-matrix systematic uncertainty. This systematic error is in principle asymmetric because both $(dN/dE_x)_{R^-}$ and $(dN/dE_x)_{R^+}$ could lie on the same side of $(dN/dE_x)_{R^0}$, the final-state distribution inferred from the $R = 4.5$ fm analysis (recall that all three final-state distributions must have the same area).

The energy-calibration systematic error was found by rebinning our delayed-α data with high and low energy calibrations differing by $\pm 1\sigma$ from the central calibration, taking account of the full covariance matrix from fitting the energy-calibration data. We then made R-matrix analyses of these high and low spectra, which again had the same

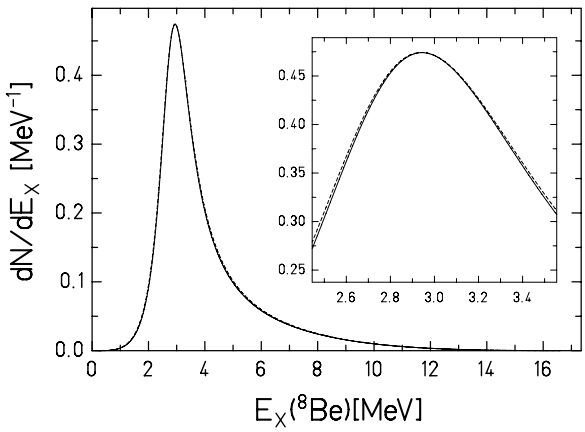

FIG. 11. Comparison of the ^{8}B final-state continuum shapes we extract from R-matrix analyses of our α spectrum (solid curve) and previous spectrum of Wilkinson and Alburger [7] (dashed). Both shapes have been normalized to the same total area. The agreement is remarkably good.

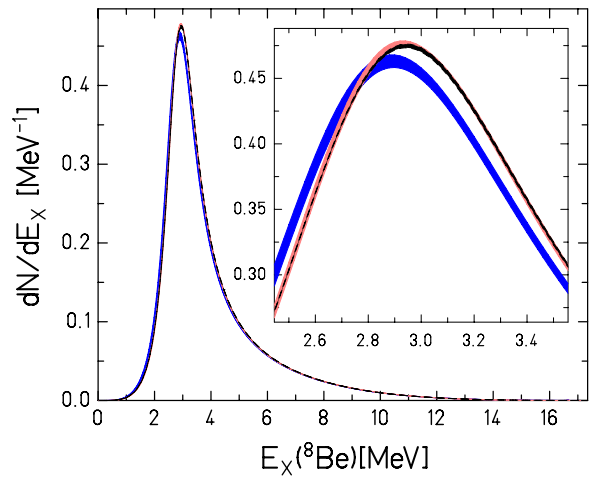

FIG. 12. (Color online) Comparison of ^{8}B final-state continuum shapes from our work (narrow black curve) to recent results from Ortiz *et al.* [16] (broad blue band) and Winter *et al.* [18] (narrow light-red band). The shaded bands show $\pm 1\sigma$ error bands of the R-matrix final-state distribution. All shapes have been normalized to the same total area. Our results and those of Winter *et al.* overlap to such a degree that they are nearly indistinguishable in this plot. Our $\pm 1\sigma$ error band was computed as described in the text. We generated the error band for the Ortiz *et al.* data from our R-matrix fits to their $\pm 1\sigma$ spectra. The Winter *et al.* error band was generated by distorting the energy scale with a multiplicative factor of $1 \pm (0.275\%)$ added in quadrature with a constant offset of 3 keV as described in Ref. [18].

TABLE II. Comparison of ^{8}B β-decay R-matrix parameters extracted from this and other recent works. Energies and widths are in keV, GT matrix elements are in μ_N. E_2 and E_3 and the reduced widths γ_2^2 and γ_3^2 were fixed at values derived from Ref. [22]. All analyses use the R-matrix formalism of Ref. [11].

Param.	This Work	Ref. [11]	Ref. [16]	Ref. [18]
E_1	$3037 \pm 5 \pm 1$	3063 ± 4	3012 ± 12	3043
γ_1^2	$1075 \pm 6 \pm 3$	1148 ± 6	1179 ± 18	1087
M_1	$-0.1449 \pm 0.0006 \pm 0.0001$	-0.1507 ± 0.0005	-0.1476 ± 0.0015	-0.1462
E_2	16626	16626	16626	16626
γ_2^2	10.89	10.89	10.89	10.96
E_3	16922	16922	16922	16922
γ_3^2	7.46	7.46	7.46	7.42
M_{2+3}	$3.152 \pm 0.158 \pm 0.009$	2.377 ± 0.100	3.555 ± 0.430	2.423
E_4	37000	37000	37000	37000
γ_4^2	$7099 \pm 276 \pm 12$	5660 ± 242	7756 ± 681	5619
M_4	$-0.254 \pm 0.022 \pm 0.001$	-0.133 ± 0.020	-0.332 ± 0.05	-0.132

total number of counts as the spectrum based on the best-fit energy calibration. Energy-calibration systematic errors were obtained from the $(dN/dE_x)_{E^+}$ and $(dN/dE_x)_{E^-}$ final-state distributions inferred from R-matrix fits to the high and low spectra. These systematic errors were again, in principle, asymmetrical. For simplicity, we adopted symmetric measures of the R-matrix and energy-calibration uncertainties, in each case the larger of the two $\pm 1\sigma$ asymmetric uncertainties. We recommend that the R-matrix and energy-calibration uncertainties be added in quadrature to obtain the total uncertainty in the final-state distribution.

E. Comparison with previous delayed-α final-state distributions

1. Wilkinson-Alburger data

Figures 10 and 11 compare our new measurements of the final-state distributions in ^{8}Li and ^{8}B decays with the corresponding quantities from our reanalysis [11] of the Wilkinson-Alburger thin-catcher data. We cannot show realistic error bands for this comparison because the covariance matrix of the energy calibration for the Wilkinson-Alburger data is not available. Nevertheless, the reanalyzed Wilkinson-Alburger data agree well with our results, being well within the ± 60 keV uncertainty in E_x (± 30 keV in E_α quoted in Ref. [14]). The concordance of the ^{8}B results is particularly impressive. During the course of this work, we discovered an error in the fitting program used in Ref. [11]. Correcting this error gave R-matrix parameters, shown in Table II, that differed slightly from the values quoted in Ref. [11].

2. Recent Notre Dame and LBL-ANL results

Two new high-precision measurements of the the ^{8}B delayed-α continuum have recently been reported. Although both results were based on detecting the summed energies of the two α's, so that the first-order effects of lepton recoil were absent, the experimental techniques were quite different. Ortiz *et al.* [15,16] at Notre Dame produced the ^{8}B with the same reaction we used, but mounted their catcher foils on a chain that carried them into a strong magnetic field that swept away the positrons, avoiding the positron summing problem. But this introduced energy-dependent distortions of the spectrum from charge-state fractionation, noncoaxial α emission, and energy losses in the detector dead layers of the obliquely incident α's, which had to be taken into account. An LBL-ANL collaboration of Winter *et al.* [17,18] implanted energetic ^{8}B ions into a Si detector where their decays were measured. This experiment had to deal with positron summing in the implantation detector and questions about the absolute energy calibration.

In contrast, our experiment was very straightforward. We minimized positron summing by employing very small detector solid angles and were able to make careful measurements of our detector resolution. The largest systematic uncertainty, the energy, was dominated by measurements of the α-source and detector dead-layer thicknesses. Unlike in the other

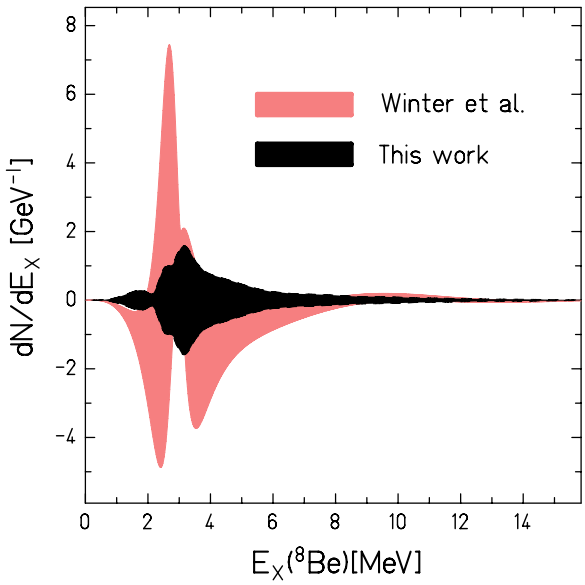

FIG. 13. (Color online) Detailed comparison of our ^{8}B final-state continuum shape (narrower black) to that of Winter *et al.* [18] (broader red). Our central value has been subtracted from both data sets. The shaded regions show the $\pm 1\sigma$ error bands of the two data sets.

TABLE III. R-matrix parameters of the ^{8}Be 2^+ continuum inferred from $L = 2$ $\alpha + \alpha$ phase shifts analyzed in Ref. [11] and from the ^{8}Li and ^{8}B delayed-α spectra reported in this work. Energies and widths are in keV, GT matrix elements are in μ_N. E_2 and E_3 and the widths Γ_2 and Γ_3 were fixed at values derived from Ref. [22]. Coulomb functions were evaluated at a radius of 4.5 fm. Unless otherwise noted, errors are formal fitting errors and do not include contributions from systematic uncertainties. For the delayed-α results the second, systematic error is from uncertainties in the energy scale.

Param.	$\alpha + \alpha$	^{8}Li	^{8}B
E_1	3049 ± 23	$3039 \pm 6 \pm 1$	$3037 \pm 5 \pm 1$
Γ_1	1395 ± 37	$1477 \pm 10 \pm 2$	$1471 \pm 6 \pm 2$
M_1		$-0.1542 \pm 0.0008 \pm 0.0001$	$-0.1449 \pm 0.0006 \pm 0.0001$
E_2	16626	16626	16626
Γ_2	108	108	108
E_3	16922	16922	16922
Γ_3	74	74	74
M_{2+3}		$2.694 \pm 0.219 \pm 0.046$	$3.152 \pm 0.158 \pm 0.009$
E_4	37000	37000	37000
γ_4^2	5347 ± 144	$5982 \pm 444 \pm 37$	$7099 \pm 276 \pm 12$
M_4		$-0.164 \pm 0.039 \pm 0.009$	$-0.254 \pm 0.022 \pm 0.001$
χ^2/ν	0.64	1.36	1.24

experiments, we had to account for the first-order effects of lepton recoil, but this can be done with little uncertainty. As a result we quote the smallest errors of the three measurements.

Figure 12 and Table II compare our ^{8}B final-state distribution to LBL-ANL and Notre Dame results. Our results agree beautifully with Winter *et al*. Both we and Winter *et al*. find that the peak in the final-state distribution is narrower and occurs about 60 keV higher in E_x than in the Notre Dame result. Figure 13 shows a detailed comparison of our work to that of Winter *et al*.

V. CONCLUSION

The increasingly precise solar neutrino data, particularly from the SNO detector, place a premium on high-quality measurements of the unoscillated or intrinsic spectrum of ^{8}B neutrinos, as the oscillation parameters are sensitive to the energy-dependent distortion of the spectrum shape. This in turn requires accurate knowledge of the shape of the very broad ^{8}Be final-state continuum fed in the decays.

Two measurements [15,17] of this continuum were recently reported, with comparably high quoted precisions. Both measurements detected the summed energies of the two alphas, so the first-order effects of lepton recoil were absent. However, the two experiments involved very different systematic effects.

This paper reports an entirely different measurement based on measuring the energies of only one of the two α's, which, of course, had completely different systematic effects from Refs. [15,17]. Beta summing was negligible, but we had to account for lepton recoil. Our main systematic effects were due to the energy resolutions of the detectors and calibration sources. Our data were taken and analyzed after the publication of Ref. [15] but before the appearance of Ref. [17]. The delay in publication resulted from our slowness in computing the ^{8}B neutrino spectrum from our final-state continuum measurements. Winter *et al*.'s calculation of the neutrino spectrum, including a careful treatment of recoil-order effects, has superseded our attempts, so we report only our measurement of the final-state continuum.

The outstanding agreement between our work and that of Refs. [17,18] and our reanalysis of Ref. [7]) is remarkable. For the first time, there is a concordance, at a high level of precision, between three independent measurements of the final-state continuum in ^{8}B decay performed by two entirely different techniques. This provides a robust basis for calculating the intrinsic neutrino spectrum from ^{8}B activity in the Sun. Because of the excellent agreement of our final-state distribution and that of Refs. [17,18], there is no need for us to present a neutrino spectrum derived from our work, as it would not differ significantly from that of Winter *et al*.

Finally, it is noteworthy that the parameters of the lowest 2^+ level in ^{8}Be inferred from our ^{8}Li and ^{8}B delayed-α data are consistent within errors, and both are quite close to the parameters inferred from the $\alpha + \alpha$ phase shifts (see Table III). The excitation energies agree within the quoted uncertainties. Although the width extracted from scattering data is about 100 keV less than the β-decay value, this could well be an artifact of a simplifying assumption inherent in the R-matrix description of the delayed-α spectra, namely that the Gamow-Teller matrix elements are strictly independent of excitation energy. This agreement, which is now substantially closer than that observed by Warburton [14], further weakens Barker's argument for a low-lying intruder state [12,13] in ^{8}Be.

ACKNOWLEDGMENTS

K. B. Swartz helped to initiate this work and took preliminary data. G. C. Harper installed and debugged the terminal ion source and built the temperature-controlled electronics rack. We thank K. A. Snover and J. F. Amsbaugh for assistance with the experiment. This work was supported in part by the U.S. Department of Energy.

[1] Y. Fukuda *et al*. (Kamiokande Collaboration), Phys. Rev. Lett. **77**, 1683 (1996).
[2] S. Fukuda *et al*. (Super-Kamiokande Collaboration), Phys. Rev. Lett. **86**, 5651 (2001).
[3] Q. R. Ahmad *et al*. (SNO Collaboration), Phys. Rev. Lett. **87**, 071301 (2001).
[4] S. N. Ahmed *et al*. (SNO Collaboration), Phys. Rev. Lett. **92**, 181301 (2004).
[5] B. T. Cleveland *et al*., Astrophys. J. **496**, 505 (1998).
[6] J. N. Bahcall, E. Lisi, D. E. Alburger, L. DeBraeckeleer, S. J. Freedman, and J. Napolitano, Phys. Rev. C **54**, 411 (1996).
[7] D. H. Wilkinson and D. E. Alburger, Phys. Rev. Lett. **26**, 1127 (1971).
[8] B. J. Farmer and C. M. Class, Nucl. Phys. **15**, 626 (1960).
[9] L. DeBraeckleer and D. Wright, unpublished data.
[10] J. Napolitano, S. J. Freedman, and J. Camp, Phys. Rev. C **36**, 298 (1987).
[11] M. Bhattacharya and E. G. Adelberger, Phys. Rev. C **65**, 055502 (2002).
[12] F. C. Barker, Aust. J. Phys. **22**, 293 (1969).
[13] F. C. Barker, Aust. J. Phys. **42**, 25 (1989).
[14] E. K. Warburton, Phys. Rev. C **33**, 303 (1986).
[15] C. E. Ortz, A. Garcia, R. A. Waltz, M. Bhattacharya, and A. K. Komives, Phys. Rev. Lett. **85**, 2909 (2000).
[16] C. E. Ortiz, Ph.D. thesis, University of Notre Dame 2000.
[17] W. T. Winter, S. J. Freedman, K. E. Rehm, I. Ahmad, J. P. Greene, A. Heinz, D. Henderson, R. V. F. Janssens, C. L. Jiang, E. F. Moore, G. Mukherjee, R. C. Pardo, T. Pennington, G. Savard, J. P. Schiffer, D. Seweryniak, G. Zinkann, and M. Paul, Phys. Rev. Lett. **91**, 252501 (2003).
[18] W. T. Winter, S. J. Freedman, K. E. Rehm, and J. P. Schiffer, Phys. Rev. C **73**, 025503 (2006), arXiv:nucl-ex/0406019.
[19] K. B. Swartz, Ph.D. thesis, University of Washington, 1996.
[20] North American Scientific, 20200 Sunburst Street, Chatsworth, CA 91311.
[21] A. Rytz, At. Data Nucl. Data Tables **49**, 205 (1991).
[22] F. Ajzenberg-Selove, Nucl. Phys. **A413**, 1 (1984).
[23] D. H. Wilkinson and B. E. F. Macefield, Nucl. Phys. **A232**, 58 (1974).
[24] See EPAPS Document No. E-PRVCAN-73-003606 for files containing ^{8}B and ^{8}Li final state distributions at 20 keV intervals. For more information on EPAPS, see http://www.aip.org/pubservs/epaps.html.